

Slidable Cross-Linking Effect on Liquid Crystal Elastomers: Enhancement of Toughness, Shape-Memory, and Self-Healing Properties

Subi Choi, Bitgaram Kim, Sungmin Park, Ji-Hun Seo,* and Suk-kyun Ahn*



Cite This: *ACS Appl. Mater. Interfaces* 2022, 14, 32486–32496



Read Online

ACCESS |



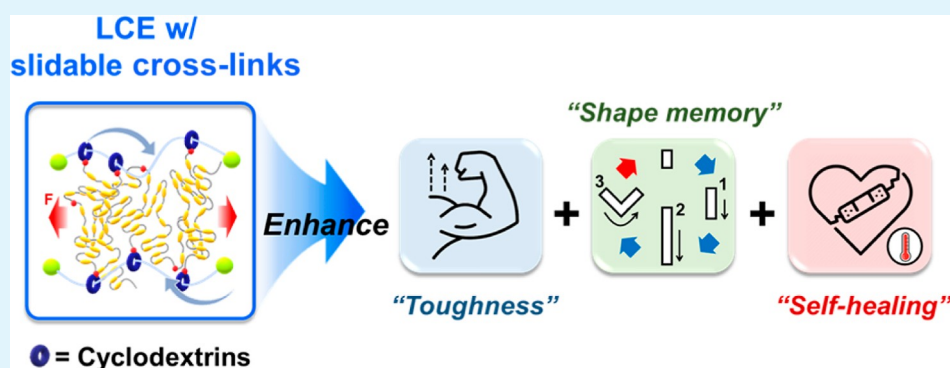
Metrics & More



Article Recommendations



Supporting Information



ABSTRACT: The network structures of liquid crystal elastomers (LCEs) are crucial to impart rubbery behavior to LCEs and enable reversible actuation. Most LCEs developed to date are covalently linked, implying that the cross-links are fixed at a particular position. Herein, we report a new class of LCEs integrating polyrotaxanes (PRs) as slidable cross-links (PR-LCEs). Interestingly, the incorporation of a low loading (0.3–2.0 wt %) of the PR cross-linkers to the LCE causes a significant impact on various properties of the resulting PR-LCEs due to the pulley effect. The optimum PR loading is determined to be 0.5 wt %, at which point the toughness and damping behavior are maximized. The robust mechanical properties of the PR-LCE offers a superior actuation performance to that of the pristine LCE along with an excellent quadruple shape-memory effect. Furthermore, the incorporation of PR is useful to enhance the efficiency of shape-memory-assisted self-healing when heating above the nematic–isotropic transition.

KEYWORDS: liquid crystal elastomers, polyrotaxanes, shape-memory polymers, self-healing, actuators

INTRODUCTION

Liquid crystal elastomers (LCEs) undergo spontaneous shape transformations in response to various external stimuli, such as heat, light, and humidity, due to a change in the molecular ordering.^{1–6} The large actuation capability up to 400% strain along with an anisotropic molecular order of LCEs has been harnessed to create a unique smart material platform and a variety of interesting devices, including soft robots,^{7–11} switchable surfaces,^{12–14} microfluidics,¹⁵ smart adhesives,¹⁶ dampers,^{17,18} and biomedical substrates.^{19–21} LCEs are lightly cross-linked through robust covalent networks, which impart rubber-like properties to them and enable effective reversible actuation. To further enhance their mechanical properties and actuating performances, LCEs consisting of dual networks have also been developed.^{22–24} Recently, various types of dynamic covalent bonds that allow LCE network rearrangement under heat or light stimuli have also been introduced, and such systems are expected to offer several benefits over conventional LCEs, such as reprocessing, shape-reconfiguration, and self-healing properties.^{25–29} However, the cross-linking points in

the LCEs developed to date remain statically fixed and thus could not be translated in the absence of external stimuli.

The incorporation of sliding cross-links into polymer networks has been demonstrated as an interesting strategy to achieve high stretchability and mechanical elasticity, in addition to promoting self-healing.^{30–33} For example, the introduction of polyrotaxanes (PRs) constitutes a representative method in the development of slidable polymer networks.³⁴ PRs are necklace-like supramolecules in which cyclodextrins (CDs) are threaded onto linear polymer chains that are capped with bulky end groups. The CD rings can slide along the polymer axis, especially during loading and unloading, which can equalize the applied load in a manner

Received: April 12, 2022

Accepted: June 27, 2022

Published: July 6, 2022



similar to a pulley. Through this so-called “pulley effect” at the molecular level,³⁵ such PR-containing materials can exhibit enhanced stretchability and toughness as demonstrated in hydrogels,³⁶ glassy polymers,³⁷ polymer electrolytes,³⁸ and elastomers.^{39–41}

Thus, we herein report the synthesis of a new series of dynamic LCEs incorporating supramolecular PR (PR-LCEs) by linking diacrylate-terminated LC oligomers with multi-acrylate-functionalized PRs as slidable cross-linkers, in addition to a subsequent exploration of their thermal, mechanical, and actuation properties. To the best of our knowledge, this is the first investigation that even a small PR loading (0.3–2.0 wt %) in LCEs can bring a significant impact on the mechanical and viscoelastic properties compared to the non-PR-LCE counterpart while preserving the intrinsic shape-transformation characteristics of the LCEs. In addition, the tensile strength and toughness are optimized to improve the shape-memory and actuation performances of the resulting PR-LCEs. Furthermore, the influence of the slidable cross-linker motility on the self-healing efficiency over the pristine LCE is examined under the same heating conditions.

■ EXPERIMENTAL SECTION

Synthesis of LCE-Containing PR Cross-Linkers. The liquid crystal oligomer (LCO) and the PR were synthesized separately following procedures described in our earlier publications,^{42,43} and their detailed synthetic protocols as well as their characterization results can be found in the [Supporting Information](#). The PR was dissolved in chloroform to prepare a stock solution with a concentration of 1.5×10^{-5} M; then, a desired amount in the PR solution was transferred to a vial containing the LC oligomer and mixed using a heat gun and a vortex. Subsequently, the mixture was cast onto a glass Petri dish and placed in a vacuum oven at 80 °C (nematic state) for 3 h to remove the solvent. Afterward, the desired amount of the PR-LCO mixture was placed between two glass slides pre-cleaned with acetone, and 100 μ m aluminum spacers were inserted between the glass slides to control the sample thickness. The PR-LCO mixture was then hot-pressed by applying a gentle pressure (1 MPa) at 80 °C (nematic state), and the pressed PR-LCO mixture was exposed to UV light (OmniCure S1500, $\lambda = 365$ nm, 38 mW cm^{-2}) for 30 min at room temperature for photocross-linking. Preparation details for the mechanically programed LCEs can be found in the [Supporting Information](#).

Materials Characterization. The ^1H NMR spectra were recorded on a 500 MHz Varian spectrophotometer using CDCl_3 as a solvent. A polarizing optical microscope (Nikon Eclipse LV100N POL) equipped with a heating stage (Linkam LTS420) was used to identify the LC phase, the phase transition, and alignment and to evaluate the thermal actuation of the LCEs using ToupView software. Differential scanning calorimetry (DSC, TA Instruments, Discovery DSC25) was performed under nitrogen flow; the samples were heated to 150 °C, then cooled to –50 °C, and then reheated to 150 °C at a rate of 10 °C min^{-1} . Atomic force microscopy (AFM, Park XE-7 from Park Systems) was used to examine the surface topographies and phase images over 10 $\mu\text{m} \times 10 \mu\text{m}$ areas of the LCEs in the non-contact mode at a scan rate of 1.5 Hz (PPP-NCHR AFM probe, $k = \sim 42$ N m^{-1} , $f = \sim 330$ kHz). AFM imaging was conducted at 30 °C under a 40% relative humidity, and XEI software (version 4.34) was used for data processing. A laser scanning confocal microscope (Olympus OLS5000) equipped with a heating stage was used to characterize the thermal actuation of the LCE microdimples and the self-healing process of the damaged LCEs. When characterizing the samples using a heating stage, the cover of the heating stage had to be removed, and therefore the temperature was calibrated using a thermocouple after the measurement.

Gel Fraction. All the samples were immersed in chloroform for 48 h to extract the un-cross-linked components and then dried in a

vacuum oven for 24 h at room temperature. The mass of the sample before and after extraction was measured, and the gel fraction (G) was calculated using following eq 1

$$G (\%) = \frac{m_f}{m_i} \times 100 (\%) \quad (1)$$

where m_i is the initial mass of the sample before extraction and m_f is the final dried mass of the sample after extraction and drying.

X-ray Scattering. The small- and wide-angle X-ray scattering (SAXS and WAXS) measurements were performed at the 9A U-SAXS beamline of the Pohang Accelerator Laboratory (PAL), Korea. The 2D scattering patterns were recorded using a 2D CCD detector (Rayonix MX170-HS), which was located 2.05 and 0.22 m away from the sample for SAXS and WAXS, respectively. The 1D intensity profiles versus the scattering vector $q = (4\pi/\lambda) \sin(\theta/2)$ were obtained from the 2D patterns, where θ is the scattering angle and $\lambda = 1.119$ Å ($E = 11.07$ keV) represents the X-ray wavelength. The order parameter (S) was calculated using the following Hermans-Stein orientation distribution function (2 and 3)

$$S = \frac{3\langle \cos^2 \theta \rangle - 1}{2} \quad (2)$$

$$\langle \cos^2 \theta \rangle = \frac{\int_0^{\pi/2} I(\theta) \sin \theta \cos^2 \theta d\theta}{\int_0^{\pi/2} I(\theta) \sin \theta d\theta} \quad (3)$$

where θ is the azimuthal angle and $I(\theta)$ is the θ -dependent intensity at $q_i = 1.41$ Å. The value of q_i corresponds to the position of the maximum in the WAXS 1D profile, which indicates the intermolecular distance between the LCEs and the PR-LCEs.

Mechanical and Viscoelastic Properties. A dynamic mechanical analyzer (TA instruments, DMA Q850) was used to characterize the stress–strain responses and the temperature-dependent viscoelastic properties in the tensile mode. For the stress–strain measurements, all samples were equilibrated at room temperature under a preload of 1 mN, and the force was increased at a rate of 0.2 N min^{-1} . Rectangular specimens were prepared with dimensions of 7.0 mm (L) \times 4.0 mm (W) \times 0.1 mm (T) for the polydomain LCEs and 5.0 mm (L) \times 2.5 mm (W) \times 0.1 mm (T) for the monodomain LCEs. For the viscoelastic measurements, the polydomain LCEs with dimensions of 7.0 mm (L) \times 5.0 mm (W) \times 0.1 mm (T) were heated from –50 to 150 °C at a rate of 3 °C min^{-1} under 14 μm amplitude at a constant frequency of 1 Hz. The values of T_g were determined from the first peak observed in the $\tan \delta$ curve.

One-Way Shape-Memory Properties. The cyclic thermomechanical shape-memory cycle was programed using dynamic mechanical analysis (DMA) with a controlled force mode and a tension film clamp. A rectangular specimen of the polydomain LCE was prepared with dimensions of 7.0 mm (L) \times 5.0 mm (W) \times 0.1 mm (T), and the quadruple shape-memory cycle was created according to the following protocol. Initially, the sample was equilibrated at 150 °C for 3 min. (1) To obtain the first temporary shape (B or ϵ_B), the sample was elongated at 150 °C by ramping the force from the preload (1 mN) to 0.006 N at a rate of 0.006 N min^{-1} . The sample was then cooled to 85 °C at a rate of 3 °C min^{-1} under a constant force (0.006 N) and equilibrated for 20 min. The force applied to the sample was then unloaded to reach the preload value (1 mN) at a rate of 0.006 N min^{-1} . (2) To obtain the second temporary shape (C or ϵ_C), the sample was elongated at 85 °C by ramping the force to 0.015 N at a rate of 0.006 N min^{-1} . Subsequently, the sample was cooled to 30 °C at a rate of 3 °C min^{-1} under a constant force (0.015 N) and equilibrated for 20 min. The force applied to the sample was then unloaded to the preload value (1 mN) at a rate of 0.006 N min^{-1} . (3) To obtain the third temporary shape (D or ϵ_D), the sample was elongated at 30 °C by ramping the force to 0.05 N at a rate of 0.006 N min^{-1} . Subsequently, the sample was cooled to 0 °C at a rate of 3 °C min^{-1} under a constant force (0.05 N) and equilibrated for 20 min. The force applied to the sample was then unloaded to the preload value (1 mN) at a rate of 0.006 N min^{-1} . (4) Finally, to

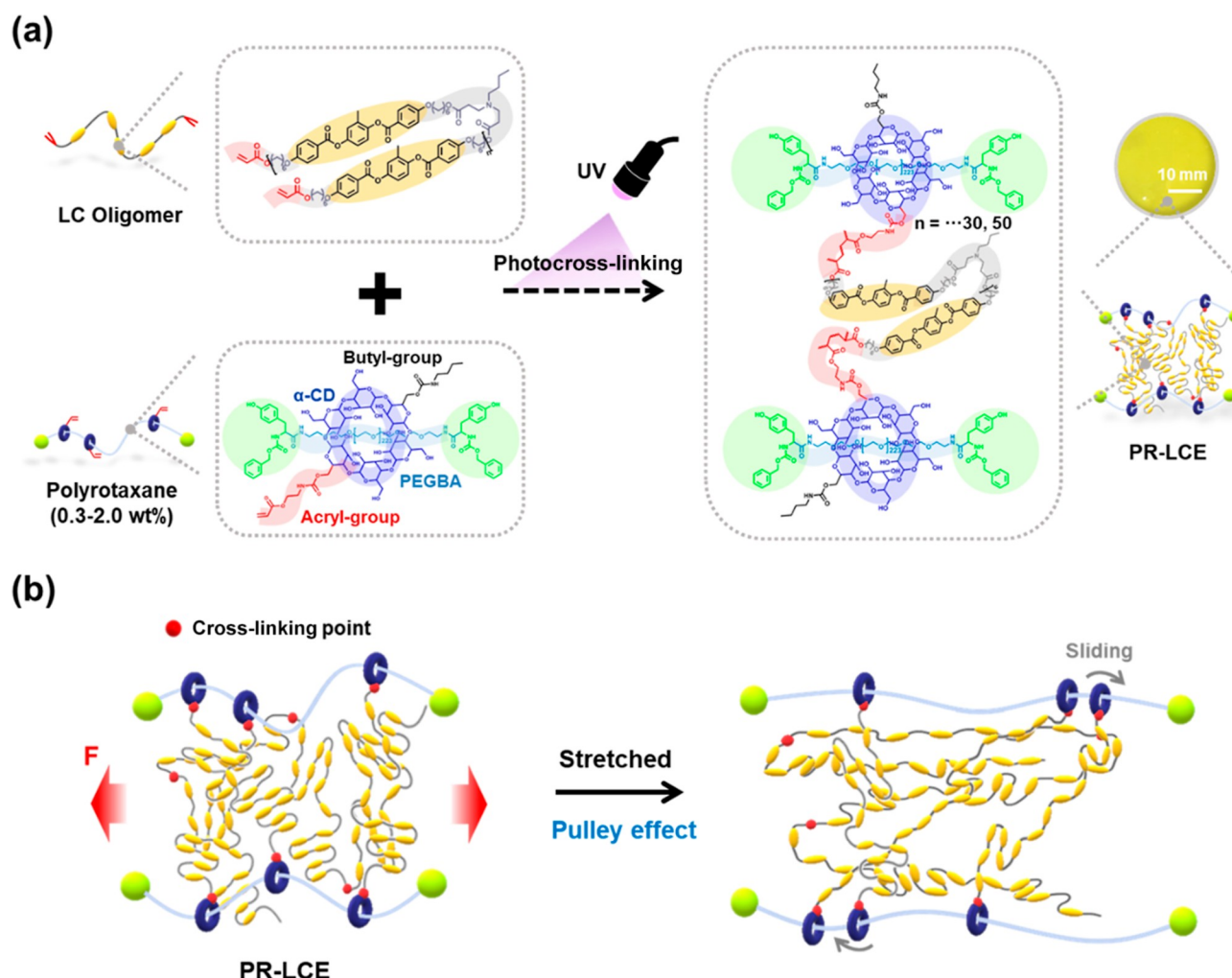


Figure 1. (a) Schematic representation of the photocross-linking reaction of PR-LCE and (b) sliding behavior of α -CDs in the PR-LCE upon stretching.

recover the permanent shapes (C_{rec} , B_{rec} , and A_{rec} or $\epsilon_{C,rec}$, $\epsilon_{B,rec}$, and $\epsilon_{A,rec}$), the sample was heated first to 30 °C and equilibrated for 20 min, then to 85 °C and equilibrated for 20 min, and finally to 150 °C and equilibrated for 20 min; these heating processes were carried out at a rate of 3 °C min⁻¹. This procedure was repeated twice more on the same sample. The quantitative shape-memory properties, including the strain, the shape fixity ratio (R_f), and the shape recovery ratio (R_r), were then determined by analyzing the results of the cyclic thermomechanical measurements. R_f and R_r were calculated according to the following eqs 4 and 5

$$R_f (X \rightarrow Y) = \frac{\epsilon_y - \epsilon_x}{\epsilon_{y,load} - \epsilon_x} \times 100 (\%) \quad (4)$$

$$R_r (Y \rightarrow X) = \frac{\epsilon_y - \epsilon_{x,rec}}{\epsilon_y - \epsilon_x} \times 100 (\%) \quad (5)$$

where X and Y denote two different shapes, respectively, $\epsilon_{y,load}$ is the maximum strain under a load before unloading, ϵ_x and ϵ_y are the strains after cooling and unloading, respectively, and $\epsilon_{x,rec}$ is the strain after recovery.

Reversible Actuation. A monodomain LCE floated on a small drop of silicon oil was placed on a glass slide, and the dimensional change of the LCE as a function of temperature was monitored under POM using a heating stage. To evaluate the actuation performance of the various LCEs, DMA was employed using a tension film clamp. The monodomain LCEs [10 mm (L) \times 2.5 mm (W) \times 0.1 mm (T)] were heated from 30 to 180 °C under the isostress mode (a preload of

1 mN) or under the isostrain mode (a strain of 0.001%) at a rate of 10 °C min⁻¹ to determine the actuation strain or stress, respectively. To determine the stability during thermal actuation, the monodomain sample [10 mm (L) \times 2.5 mm (W) \times 0.1 mm (T)] was heated and cooled between 20 and 120 °C under a preload of 1 mN at a rate of 5 °C min⁻¹ in the controlled force mode. This temperature cycling test was repeated 20 times on the same sample.

Work Capacity. To evaluate the work capacity, the polydomain LCE samples [7 mm (L) \times 4.0 mm (W) \times 0.1 mm (T)] were equilibrated at an isotropic state (120 °C) in the controlled stress mode. Subsequently, the samples were cooled from 120 to -50 °C at a rate of 3 °C min⁻¹ under a constant bias stress (100 kPa). Finally, the volumetric work capacity was calculated using following eq 6

$$\text{work capacity} = \frac{W}{V} = \frac{F_{bias} \Delta L}{LWT} = \frac{F_{bias}}{A} \times \frac{\Delta L}{L} = \sigma_{bias} \times \epsilon \quad (6)$$

RESULTS AND DISCUSSION

Synthesis of LCEs Incorporating Slidable Cross-Linkers. The aim of this study is to investigate the impact of a PR cross-linker on the viscoelastic, mechanical, shape-memory, actuation, and self-healing properties of LCEs. To prepare a model LCE system, a diacrylate-terminated poly(β -amino ester) type LCO was initially synthesized based on a previous literature method (Figure S1, Supporting Informa-

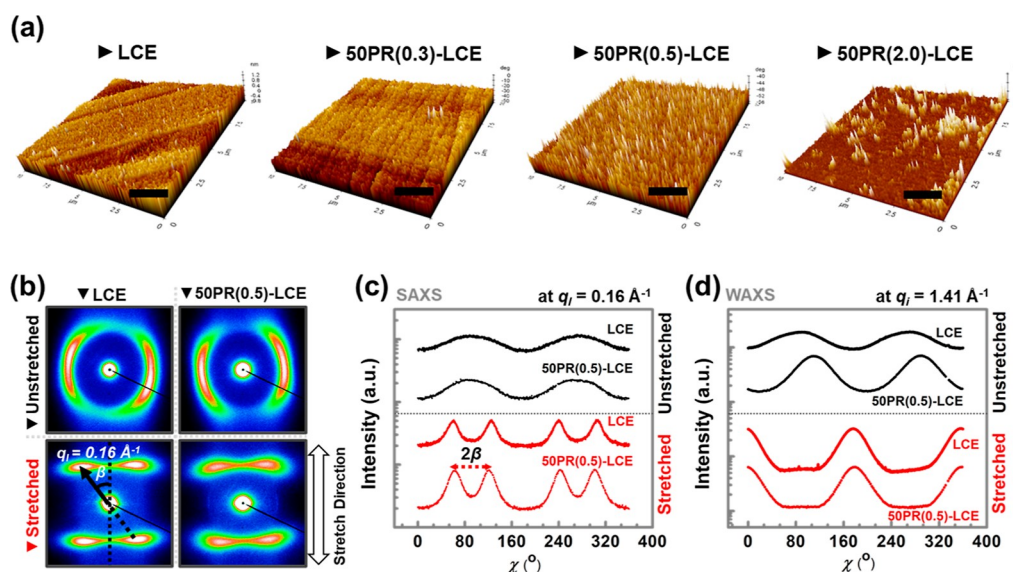


Figure 2. (a) AFM phase images of the LCE and the PR-LCEs. Scale bars represent $2 \mu\text{m}$. (b) 2D SAXS patterns, (c) 1D azimuthal scan profiles at $q_1 = 0.16 \text{ \AA}^{-1}$ (i.e., SAXS), and (d) 1D azimuthal scan profiles at $q_1 = 1.41 \text{ \AA}^{-1}$ (i.e., WAXS) of the LCE and 50PR(0.5)-LCE before and after $\sim 150\%$ uniaxial stretching.

Table 1. Thermal and Mechanical Properties of the LCE and the PR-LCEs

sample	T_g ($^{\circ}\text{C}$) ^a	T_{pm} ($^{\circ}\text{C}$) ^b	G (%) ^c	elastic modulus (MPa) ^d	strain (%) ^d	tensile strength (MPa) ^d	toughness (MJ/m^3) ^d
LCE	16	59	82	2 ± 0.05	167 ± 10	3 ± 0.6	1.4 ± 0.2
50PR(0.3)-LCE	20	65	85	3.6 ± 0.4	155 ± 7	5.3 ± 0.3	2.7 ± 0.1
50PR(0.5)-LCE	13	58	83	3 ± 0.1	193 ± 6	6 ± 0.4	3.3 ± 0.2
50PR(2.0)-LCE	15	62	86	1 ± 0.05	239 ± 26	1 ± 0.4	1 ± 0.5
30PR(0.3)-LCE				3 ± 0.3	214 ± 16	4.8 ± 0.4	3.3 ± 0.3
30PR(0.5)-LCE				2.4 ± 0.1	295 ± 1	2.5 ± 1	3 ± 0.8

^aDetermined from the $\tan \delta$ curve in the temperature range of 0 – 30 $^{\circ}\text{C}$. ^bDetermined from the $\tan \delta$ curve in the temperature range of 30 – 85 $^{\circ}\text{C}$.

^cDetermined by comparing the mass before and after extraction in chloroform. ^dDetermined from the stress–strain curves of the polydomain samples.

tion).⁴² The number-average molecular weight (M_n) of the resulting oligomer was 6300 g mol^{-1} , as determined by ^1H NMR end group analysis (Figure S6a, Supporting Information). Separately, a multiacrylate-functionalized PR consisting of 30 or 50 α -CD rings was synthesized according to our previously reported protocol,⁴³ and molecular characterization by ^1H NMR spectroscopy confirmed the successful replacement of the hydroxyl groups of the CD rings by acrylate groups (Figures S2–S5 and S6b, Supporting Information). Notably, a number of n -butyl groups were also introduced to the CD ring along with the acrylate groups to enhance the solubility of the resulting PR in moderately polar solvents, such as chloroform. Subsequently, solutions of LCO and the PR in chloroform were combined, homogeneously mixed, and cast onto a glass Petri dish. After removal of the solvent, the PR-LCO mixture was hot-pressed at 80 $^{\circ}\text{C}$, then photopolymerized at room temperature to yield the desired PR-LCE (Figure S7a, Supporting Information and Figure 1a,b). To investigate how the LCE properties are affected by the PR loading and the number of CD moieties on the PRs, a series of PR-LCEs were prepared by adjusting the PR weight percentage and the average number of CDs. As a control, a pristine LCE without a PR cross-linker was also prepared via the same method (i.e., hot-press and photopolymerization). Throughout this article, the PR-incorporating LCEs are denoted as $n\text{PR}(m)$ -LCE, where n and m represent the average number of α -CD moieties

($n = 30$ or 50) in the PR and the weight percentage of the PR ($m = 0.3, 0.5$, or 2.0 wt %) in the LCE, respectively.

Although uniform PR-LCO mixtures were obtained with relatively low PR loadings (i.e., 0.3 and 0.5 wt %), the mixture became heterogeneous upon increasing the PR loading 2.0 wt %, and this was attributed to agglomeration of PRs (Figure S8, Supporting Information). After photopolymerization, the PR-LCEs exhibited an opaque appearance, implying no global orientation of the LC domains (i.e., polydomain) within these samples (Figure 1a and S8, Supporting Information). Figure 2a shows the AFM phase images of the PR-LCEs prepared at different PR loadings, and these images clearly show the presence of PR agglomerates in the LCE matrix for the 50PR(2.0)-LCE sample. The domain size of PR agglomerates is 500 – 1000 nm in diameter and 15 – 30 nm in height as shown in the AFM topography image (Figure S9, Supporting Information). The gel fractions of both the pristine LCE and the various PR-LCEs were greater than 80% , thereby indicating sufficient cross-linking (Table 1).

To investigate the effect of PR incorporation on the LCE nanostructure, SAXS and WAXS measurements were conducted. To clearly identify the LC phase, the LCE and PR-LCE were uniaxially stretched by $\sim 150\%$, inducing the uniform alignment of their mesogenic domains. The cybotactic order (i.e., a nematic phase with smectic-C type fluctuations) was observed for all samples regardless of the PR loading

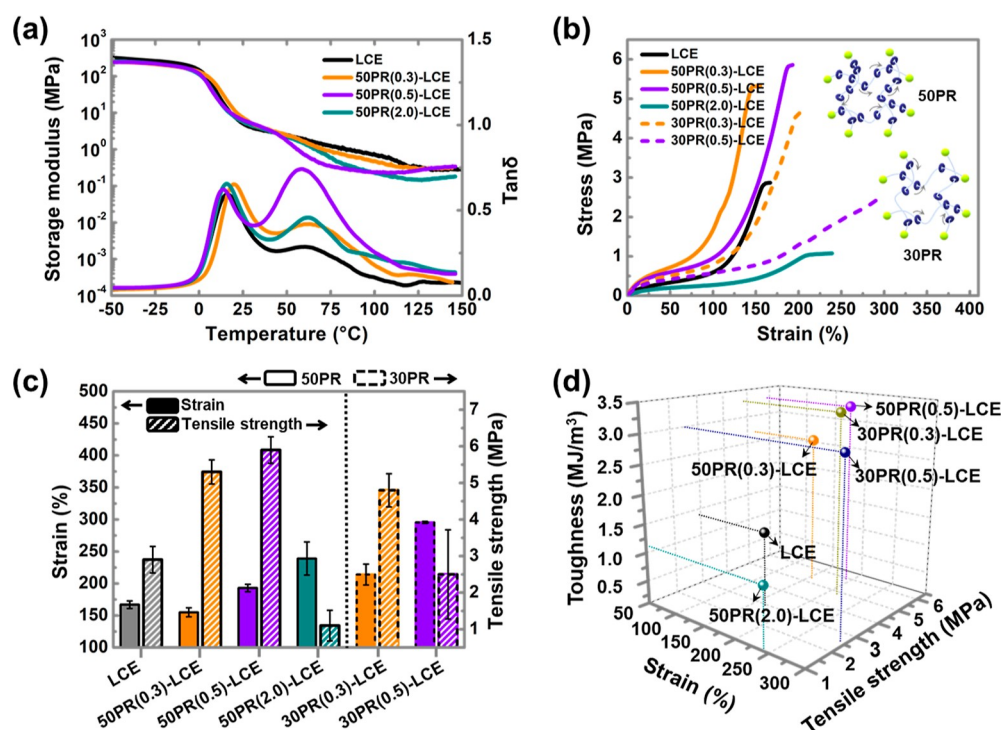


Figure 3. Viscoelastic and mechanical properties of the polydomain LCE and the PR-LCEs: (a) storage modulus and $\tan \delta$ curves during heating, (b) stress–strain curves, and (c,d) summary of the mechanical properties.

(Figure 2b and S10a, Supporting Information).⁴⁴ The layer spacing (d), the molecular tilt angle (β), and the molecular length ($L = d/\cos \beta$) was calculated for each stretched sample based on the 1D SAXS profiles (Figure 2c and S10b, Supporting Information), and the results are summarized in Table S1. From the WAXS results (Figure 2d and S10c,d, Supporting Information), the intermolecular distance (d_i) and the order parameter (S) were determined, as listed in Table S1. Overall, the microstructure and the extent of ordering of the LCE were preserved despite the incorporation of PRs into the LCE network.

Thermal, Viscoelastic, and Mechanical Properties.

The viscoelastic properties of the various LCE networks were investigated by DMA as shown in Figure 3a, and results are summarized in Table 1. The glass transition temperatures (T_g) of each LCE network was determined by the maximum peak from the corresponding $\tan \delta$ curve and was found to be in the range of 13–20 °C regardless of the PR loading, thereby indicating that the slidable cross-linker had a minimal effect on the segmental motion of the LCE. In addition, the T_g values of the LCE networks determined by DSC were observed at approximately −4 °C (Figure S11, Supporting Information).

Interestingly, additional broad peaks were observed in the $\tan \delta$ curves between 30 and 80 °C for all LCEs, and these peaks were attributed to a transition from the polydomain to the monodomain (T_{pm}).⁴⁵ This transition implies that the randomly oriented LC microdomains undergo a reorientation along the oscillating loading and become uniaxially aligned in this temperature range.⁴⁶ More interestingly, the intensities of the T_{pm} peaks of the PR-LCEs became more pronounced compared to the pristine LCE originating from the “pulley effect” of the PRs.⁴⁷ More specifically, the CDs linked in the LCE networks can slide along the poly(ethylene glycol) (PEG) backbones of the PRs when the LC domains undergo reorientation, thereby leading to a greater energy dissipation.

In addition, the energy dissipation of the PR-LCEs at T_{pm} tended to increase with an increased PR loading, as evidenced by the greater intensities of the $\tan \delta$ peaks. However, a large excess of PR [i.e., 50PR(2.0)-LCE] was found to lead to inefficient energy dissipation due to agglomeration. Above the T_{pm} , rubbery plateaus were observed, confirming the network structure. The cross-link density (ν_e) of each LCE network was calculated according to eq 7

$$\nu_e = \frac{E'}{3RT} \quad (7)$$

where E' is storage modulus at 140 °C (i.e., at the rubbery plateau), R is the gas constant, and T is the temperature (in Kelvin). The cross-linking densities of the LCE, 50PR(0.3)-LCE, 50PR(0.5)-LCE, and 50PR(2.0)-LCE were determined to be 2.7×10^{-5} , 3.0×10^{-5} , 3.2×10^{-5} , and 1.65×10^{-5} mol cm⁻³, respectively. Furthermore, the nematic–isotropic transition (T_{ni}) of each LCE network was determined by DSC to be ~106 °C (Figure S11, Supporting Information); we note that the T_{ni} in the $\tan \delta$ peak was not clearly observed likely because LCEs were cross-linked in the nematic state.⁴⁸

The mechanical properties of the various LCE network were then examined by stress–strain curves at room temperature (Figure 3b and Table 1), and the corresponding strain and tensile strength values are shown in Figure 3c, wherein several tendencies can be observed. For example, the strain of the 50PR-LCE tends to increase with an increasing PR loading, wherein the larger deformability is caused by the increased “pulley effect” at a higher PR loading, which generates a greater number of cross-links within the LCE network. As a control, we also synthesized *n*-butylated PRs containing no acrylate groups and simply blended them within the LCE matrix; these analogues are denoted as *n*BPR(*m*)-LCE. During the tensile measurements, the 50BPR-LCEs were found to be less

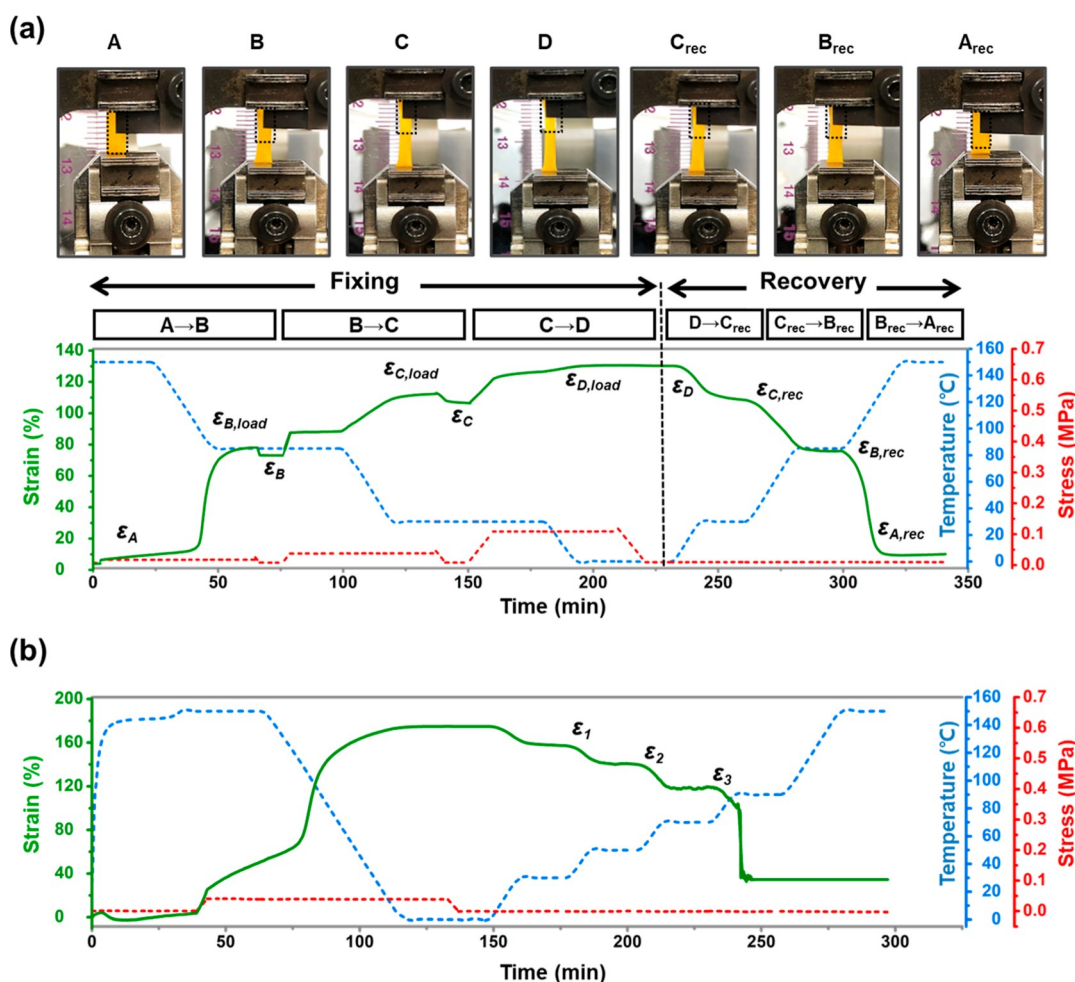


Figure 4. (a) Elongation-based one-way quadruple shape-memory effect of polydomain 50PR(0.5)-LCE: photographic images (top) and shape-memory cycles (bottom). (b) Controllable stepwise shape recovery of the polydomain 50PR(0.5)-LCE during stepwise heating.

stretchable compared to their 50PR-LCE counterparts and the pristine LCE, which suggests that the pulley effect is less effective for a physical blend of PRs and LCEs (Figure S12 and Table S2, Supporting Information). In addition, the 50PR-LCEs with a low PR loading (0.3 and 0.5 wt %) exhibited higher tensile strengths [5.3 and 6 MPa for 50PR(0.3)-LCE and 50PR(0.5)-LCE, respectively] than that of the pristine LCE (3 MPa), and their elastic modulus values increased by 3.6 and 3 MPa, respectively, compared to that of the pristine LCE (2 MPa). In contrast, both the tensile strength and the elastic modulus of the 50PR(2.0)-LCE decreased considerably (i.e., by 1 MPa) due to a pronounced pulley effect. The number of CDs incorporated into the structure was also found to affect stretchability and toughness of the PR-LCEs. Previously, it has been reported that a low CD coverage allows the CDs to slide longer distances on the PEG axis compared to the case of PRs with high CD coverages.⁴⁹ Thus, as expected, the 30PR-LCEs exhibit a greater elongation and a lower tensile strength due to a larger “pulley effect” compared to the corresponding 50PR-LCE counterparts at the same PR loading (Figure 3c). In Figure 3d, we summarize the mechanical properties of the various LCE networks, which suggests the mechanical properties can be effectively tailored by adjusting the PR concentration and the number of CDs in PRs of the LCE matrix. For the remainder of the study, we focus mainly on the properties of the 50PR(0.5)-LCE due to

the fact that it exhibited the highest toughness (i.e., $\sim 3.3 \text{ MJ m}^{-3}$) of the various LCE systems examined herein.

Shape-Memory Properties. Because LCEs are renowned as shape-transformable materials, we moved on to explore various shape-shifting properties including the one-way shape-memory effect and two-way reversible actuation. According to the DSC and DMA results, the 50PR(0.5)-LCE exhibited multiple thermal transitions, including T_g ($\sim 13^\circ\text{C}$), T_{pm} ($\sim 58^\circ\text{C}$), and T_{ni} ($\sim 100^\circ\text{C}$), thereby suggesting the potential of multiple shape-memory effects.^{50–53} Thus, we initially examined the quadruple shape-memory effect of the polydomain 50PR(0.5)-LCE by exploiting these thermal transitions. As shown in Figure 4a, three distinct programmed strains (ϵ_B , ϵ_C , and ϵ_D) are successfully obtained by the employed shape fixing procedures, namely, loading at elevated temperatures (150°C ; $T > T_{ni}$; 85°C ; $T_{pm} < T < T_{ni}$, and 30°C ; $T_g < T < T_{pm}$), and cooling and unloading at specified temperatures (85°C ; $T_{pm} < T < T_{ni}$; 30°C ; $T_g < T < T_{pm}$, and 0°C ; $T < T_g$). Interestingly, the sample underwent a spontaneous elongation (65%) during cooling from the isotropic phase (150°C) to nematic phase (85°C), which would generate a monodomain-like structure along the stretching direction. As a result, the modulus parallel to the director orientation would become higher, leading to a fairly effective shape fixing from A to B, even at 85°C which is close to T_{ni} . Each programmed strain showed effective recovery to the

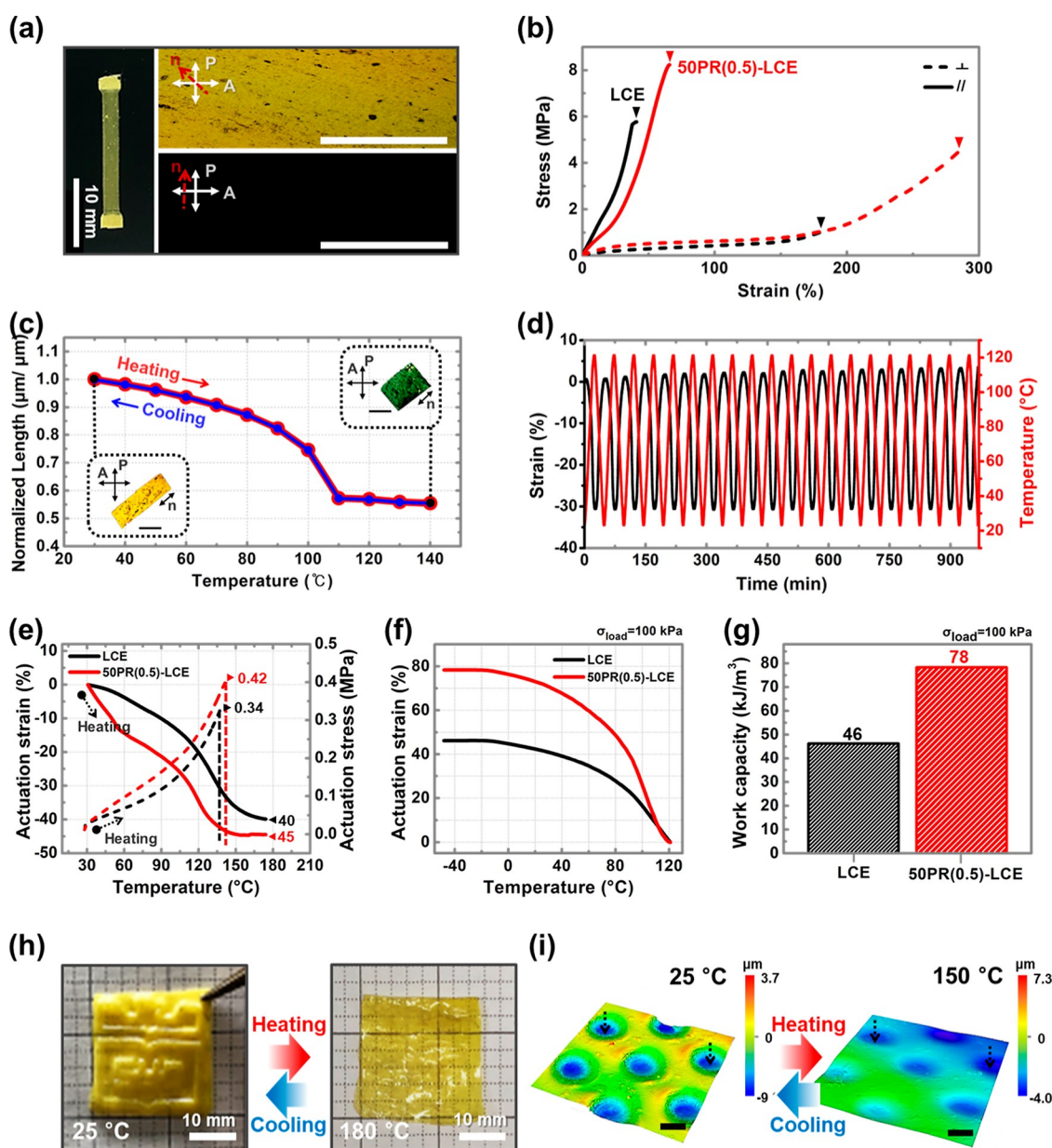


Figure 5. (a) Photographic image of a uniaxially aligned monodomain 50PR(0.5)-LCE film between crossed polarizers. POM images of the same 50PR(0.5)-LCE observed at 45° (top) and 0° (bottom) angles with respect to the cross polarizers. Scale bars represent 500 μm . (b) Stress–strain curves of the monodomain LCE and 50PR(0.5)-LCE under parallel (//) or perpendicular (\perp) loadings with respect to the nematic director. (c) Reversible actuation of the monodomain 50PR(0.5)-LCE. Scale bars represent 500 μm . (d) Reversible actuation of the monodomain 50PR(0.5)-LCE during 20 temperature cycles. (e) Actuation strain in the absence of stress and actuation stress under a constant strain (0.001%), measured for the monodomain LCE and the 50PR(0.5)-LCE. (f) Actuation strain of the polydomain LCE and the 50PR(0.5)-LCE during cooling under a constant stress (100 kPa). (g) Calculated work capacity of the polydomain LCE and the 50PR(0.5)-LCE. (h) Thermal actuation of a PNU logo-shaped 50PR(0.5)-LCE. (i) Thermal actuation of 50PR(0.5)-LCE microdimples recorded by a laser scanning confocal microscope. Scale bars represent 30 μm .

pre-programmed strain during the shape recovery process (i.e., heating in the absence of a load).

Intriguingly, we demonstrate that a T_{pm} , where randomly organized LC microdomains are uniaxially reoriented along the elongation direction or vice versa, can be harnessed as a molecular switch to trigger the shape-memory effect. While shape-memory effects based on the T_g and T_{ni} of LC polymer networks have been well documented in the literature,^{45,50,51,54–56} T_{pm} -based shape-memory effect has not been reported. Moreover, the broad transition of T_{pm} (30–85 $^{\circ}\text{C}$) of the 50PR(0.5)-LCE can be further exploited to

induce a controllable stepwise shape recovery, suggesting a supercritical behavior (Figure 4b).⁵⁷ The pristine LCE also exhibited a similar quadruple shape-memory effect (Figure S13a, Supporting Information).

The quantitative shape-memory properties of both the 50PR(0.5)-LCE and the pristine LCE were then evaluated by analyzing the strain, shape fixity (R_f), and shape recovery (R_r) ratios of the shape-memory cycles (Figure S13b,c, Supporting Information). It was observed that during the shape programming process under the same stress, the strain of the PR-LCE was 20–30% higher than that of the pristine LCE,

while the R_f and R_r values were comparable for the two samples (Figure S14a,b and Table S4, Supporting Information). The higher deformability of the PR-LCE is likely due to the “pulley effect” of PR, which agrees well with the results of the tensile measurements discussed above.

Reversible Actuation. Although the one-way shape-memory properties of polydomain PR-LCEs are valuable in terms of fixing the temporarily programmed shape, a new programming process is necessary each time to achieve the temporary shape, and the shape change between permanent and temporary shapes is not reversible.⁵⁸ To achieve reversible shape shifting, the preparation of macroscopically aligned LCEs is essential. To this end, we combined the two-step photocross-linking process with mechanical alignment by means of stretching, molding, and imprinting to prepare various types of mechanically programmed LCEs, such as a 2D film, a 3D embossed structure, and an array of microdimples (Figure S7b, Supporting Information).⁵⁹ Using this method, the uniaxially aligned monodomain 50PR(0.5)-LCE was successfully obtained, as evidenced by the brightness changes observed at different angles under POM (Figure 5a), as well as by the resulting anisotropic mechanical properties (Figure 5b and Table S3). During the tensile measurements, both the LCE and 50PR(0.5)-LCE exhibited stiff and compliant properties in parallel and in perpendicular to the nematic director, respectively. Notably, 50PR(0.5)-LCE was found to exhibit a higher tensile strength and strain in both stretching directions compared to the pristine LCE and again, this was attributed to the pulley effect, which was also observed in the stress–strain curves of the polydomain samples.

The reversible actuation was realized for the monodomain 50PR(0.5)-LCE, as it contracts and loses the birefringence upon heating above T_{ni} and recovers its initial length while cooling to room temperature (Figure 5c). As shown in Figure 5d, the reversible actuation of 50PR(0.5)-LCE under a constant stress was stable over 20 temperature cycles. In addition, upon heating to 180 °C under stress-free conditions, the 50PR(0.5)-LCE and pristine LCE display the actuation strains of 45 and 40%, respectively (Figure 5e), thereby indicating that the pulley effect contributes a slightly higher actuation strain for the 50PR(0.5)-LCE. The actuation stresses (or blocking stresses) of the monodomain LCE and 50PR(0.5)-LCE was further compared by heating the samples under constant strain (0.001%), which resulted in sample breakage at 140 and 145 °C with maximum blocking stresses of 0.34 and 0.42 MPa, respectively (Figure 5e). To further evaluate the work capacities of these samples, both samples were cooled from the isotropic state (120 °C) at 100 kPa, as shown in Figure 5f. Note that these samples were polydomain, and therefore they were spontaneously elongated to the loading direction upon cooling from the isotropic state. The calculated work capacities of the LCE and 50PR(0.5)-LCE were 46 and 78 kJ m⁻³, respectively (Figure 5g). The enhanced actuation stress and work capacity exhibited by the 50PR(0.5)-LCE was considered to originate from the stiffer and tougher characteristics of this sample compared to the pristine LCE.

In addition to the 2D film, a complex 3D-shaped LCE (embedded with the logo of Pusan National University, PNU) and an array of LCE microdimples were fabricated by molding or imprinting the partially cross-linked polydomain 50PR(0.5)-LCEs, followed by full UV curing to secure the deformed structures. When heating above T_{ni} , the protruding regions of the 50PR(0.5)-LCE-based PNU logo flattened and became

optically transparent due to a loss of LC order (Figure 5h). When the sample was cooled to room temperature, the programmed 3D structure and opaque characteristic were recovered. Similarly, the microdimples (20 μm diameter and 7 μm depth) underwent a reversible actuation during heating and cooling across T_{ni} . More specifically, the microdimple depth decrease considerably from 7 to 1 μm, although the change in diameter was marginal, as monitored by laser scanning confocal microscopy (Figure 5i and S15, Supporting Information). The reversible depth change of the microdimples in the 50PR(0.5)-LCE implies efficient local alignment of the nematic directors of the polydomain LCEs only at the regions of applied pressure. The ability to prepare macroscopically aligned PR-LCEs using various mechanical programming techniques suggests a potential to produce macro- and micro-soft actuators with enhanced mechanical properties.

Self-Healing Properties. Recently, the sliding behavior of the PR has been recognized as an interesting strategy to accelerate self-healing properties in various polymeric systems comprising reversible bonds.⁶⁰ In particular, the mobility of CDs arising from the sliding motion has been shown to assist physical self-healing.⁶¹ Therefore, we also explored the self-healing ability of 50PR(0.5)-LCE, and compared the result with that of the pristine LCE. To induce damage, the surfaces of the polydomain LCE and 50PR(0.5)-LCE (100 μm thickness) were scratched by applying the same extent of pressure using a razor blade, resulting in the generation of a ~4 μm-deep scratch (Figure S16a,b, Supporting Information). Each sample was then heated beyond its T_{ni} (150 °C) for 5 min to promote self-healing. As observed by laser scanning confocal microscopy, the scratches of 50PR(0.5)-LCE film were completely removed, whereas residual scratches remained visible in the pristine LCE film, thereby indicating incomplete healing (i.e., ~80%, Figure 6a). The mechanical properties of

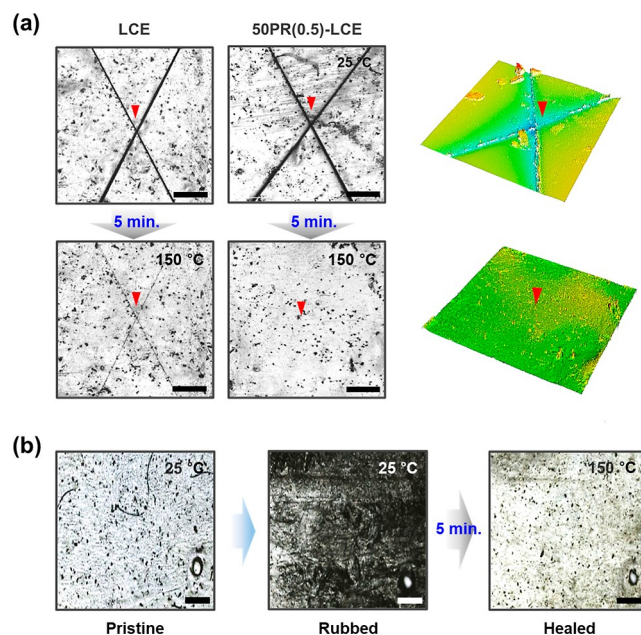


Figure 6. (a) Self-healing of the polydomain LCE and the 50PR(0.5)-LCE on scratched surfaces. Scale bars represent 500 μm. The green images (right) show the 3D topographies of the 50PR(0.5)-LCE before and after healing. (b) Self-healing of the polydomain 50PR(0.5)-LCE on a broad surface rubbed with a sandpaper. Scale bars represent 50 μm.

the scratched 50PR(0.5)-LCE film was nearly restored with self-healing efficiency of 88%, based on tensile strength values (Figure S17, Supporting Information). The excellent self-healing ability of the 50PR(0.5)-LCE was further demonstrated over a broader area by scraping the surface with sandpaper, followed by heating above T_{ni} for 5 min (Figure 6b). Overall, it was found that the effective self-healing of the 50PR(0.5)-LCE required elevated temperatures above T_{ni} , and this process was inefficient at ambient temperature due to the slower chain segmental motion and the restricted sliding motion of the CD rings (Figure S18, Supporting Information). Based on our observations, the intrinsic (partial) self-healing of the LCEs perhaps originates from the shape changing ability at T_{ni} , which is similar to the so-called shape-memory-assisted self-healing process,⁶² and this process is more effective when promoted by the sliding motion of the CD rings.

CONCLUSIONS

In summary, we synthesized a new class of LCEs by incorporating supramolecular PRs through the linking of a diacrylate-terminated LCE precursor (the LC oligomer) with a multiacrylate-functionalized PR cross-linker through photopolymerization. Interestingly, even a small loading (i.e., 0.3–2.0 wt %) of the slidable PR cross-linker resulted in significant alterations of the viscoelastic and mechanical properties of the resulting PR-LCEs, and these effects were attributed to the molecular pulley effect. However, thermal transitions (T_g and T_{ni}) of the PR-LCEs were relatively unaffected; thus, the excellent thermally induced shape changing properties of the materials, such as one-way quadruple shape-memory effect and reversible actuation, were preserved. The optimum loading of the PRs was suggested to be 0.5 wt %, because this loading resulted in the highest toughness and damping properties, and the resulting 50PR(0.5)LCE exhibited an enhanced actuation performance compared to that of the pristine LCE. Finally, we further demonstrated that the sliding effect of the PRs can be exploited to improve the efficiency of shape-memory-assisted self-healing. The synthesis of a unique series of LCEs with slide-ring cross-links and their structure–property investigation may provide useful guidelines for the creation of mechanically robust and self-healable soft actuators with extraordinary damping properties.

ASSOCIATED CONTENT

Supporting Information

The Supporting Information is available free of charge at <https://pubs.acs.org/doi/10.1021/acsami.2c06462>.

¹H NMR spectra, preparation process for samples, AFM topography analysis, XRD analysis, DSC thermograms, S–S curves for DMA, characterization of quadruple shape-memory property, and laser scanning confocal microscopy images (PDF)

Thermal actuation video (MP4)

AUTHOR INFORMATION

Corresponding Authors

Ji-Hun Seo – Department of Materials Science and Engineering, Korea University, Seoul 02841, Republic of Korea; orcid.org/0000-0001-6193-4008; Email: seojh79@korea.ac.kr

Suk-kyun Ahn – Department of Polymer Science and Engineering, Pusan National University, Busan 46241,

Republic of Korea; orcid.org/0000-0002-6841-4213;

Email: skahn@pusan.ac.kr

Authors

Subi Choi – Department of Polymer Science and Engineering, Pusan National University, Busan 46241, Republic of Korea

Bitgaram Kim – Department of Materials Science and Engineering, Korea University, Seoul 02841, Republic of Korea

Sungmin Park – Advanced Materials Division, Korea Research Institute of Chemical Technology, Daejeon 34114, Republic of Korea; orcid.org/0000-0003-4507-2959

Complete contact information is available at:

<https://pubs.acs.org/doi/10.1021/acsami.2c06462>

Author Contributions

The manuscript was written through contributions of all authors. All authors have given approval to the final version of the manuscript.

Notes

The authors declare no competing financial interest.

ACKNOWLEDGMENTS

This work was supported by National Research Foundation of Korea (NRF) grants funded by the Korean Government, Ministry of Science and ICT (MSIT) (2019R1C1C1006048, 2019M3D1A2103918, and 2021M3H4A1A03041403). S.C. acknowledges the BK FOUR Program for partial financial support. We thank Prof. Songkil Kim for carrying out the AFM measurements with the support of the PNU Hybrid Innovative Manufacturing Engineering Center.

REFERENCES

- (1) Herbert, K. M.; Fowler, H. E.; McCracken, J. M.; Schlafmann, K. R.; Koch, J. A.; White, T. J. Synthesis and Alignment of Liquid Crystalline Elastomers. *Nat. Rev. Mater.* **2022**, 7, 23–38.
- (2) Ula, S. W.; Traugott, N. A.; Volpe, R. H.; Patel, R. R.; Yu, K.; Yakacki, C. M. Liquid Crystal Elastomers: an Introduction and Review of Emerging Technologies. *Liq. Cryst. Rev.* **2018**, 6, 78–107.
- (3) Kularatne, R. S.; Kim, H.; Boothby, J. M.; Ware, T. H. Liquid Crystal Elastomer Actuators: Synthesis, Alignment, and Applications. *J. Polym. Sci., Part B: Polym. Phys.* **2017**, 55, 395–411.
- (4) White, T. J.; Broer, D. J. Programmable and Adaptive Mechanics with Liquid Crystal Polymer Networks and Elastomers. *Nat. Mater.* **2015**, 14, 1087–1098.
- (5) Ware, T. H.; McConney, M. E.; Wie, J. J.; Tondiglia, V. P.; White, T. J. Voxlated Liquid Crystal Elastomers. *Science* **2015**, 347, 982–984.
- (6) Ahn, S. k.; Ware, T. H.; Lee, K. M.; Tondiglia, V. P.; White, T. J. Photoinduced Topographical Feature Development in Blueprinted Azobenzene-Functionalized Liquid Crystalline Elastomers. *Adv. Funct. Mater.* **2016**, 26, 5819–5826.
- (7) Xiao, Y.-Y.; Jiang, Z.-C.; Zhao, Y. Liquid Crystal Polymer-Based Soft Robots. *Adv. Intell. Syst.* **2020**, 2, 2000148.
- (8) Sun, D.; Zhang, J.; Li, H.; Shi, Z.; Meng, Q.; Liu, S.; Chen, J.; Liu, X. Toward Application of Liquid Crystalline Elastomer for Smart Robotics: State of the Art and Challenges. *Polymers* **2021**, 13, 1889.
- (9) Zeng, H.; Wasylczyk, P.; Wiersma, D. S.; Priimagi, A. Light Robots: Bridging the Gap between Microrobotics and Photomechanics in Soft Materials. *Adv. Mater.* **2018**, 30, 1703554.
- (10) He, Q.; Wang, Z.; Wang, Y.; Minori, A.; Tolley, M. T.; Cai, S. Electrically Controlled Liquid Crystal Elastomer-Based Soft Tubular Actuator with Multimodal Actuation. *Sci. Adv.* **2019**, 5, No. eaax5746.
- (11) Kotikian, A.; McMahan, C.; Davidson, E. C.; Muhammad, J. M.; Weeks, R. D.; Daraio, C.; Lewis, J. A. Untethered Soft Robotic

- Matter with Passive Control of Shape Morphing and Propulsion. *Sci. Robot.* **2019**, *4*, No. eaax7044.
- (12) Liu, D.; Broer, D. J. Liquid Crystal Polymer Networks: Switchable Surface Topographies. *Liq. Cryst. Rev.* **2013**, *1*, 20–28.
- (13) Visschers, F. L. L.; Hendriks, M.; Zhan, Y.; Liu, D. Liquid Crystal Polymers with Motile Surfaces. *Soft Matter* **2018**, *14*, 4898–4912.
- (14) Babakhanova, G.; Turiv, T.; Guo, Y.; Hendriks, M.; Wei, Q.-H.; Schenning, A. P. H. J.; Broer, D. J.; Lavrentovich, O. D. Liquid Crystal Elastomer Coatings with Programmed Response of Surface Profile. *Nat. Commun.* **2018**, *9*, 456.
- (15) Lv, J.-a.; Liu, Y.; Wei, J.; Chen, E.; Qin, L.; Yu, Y. Photocontrol of Fluid Slugs in Liquid Crystal Polymer Microactuators. *Nature* **2016**, *537*, 179–184.
- (16) Ohzono, T.; Saed, M. O.; Terentjev, E. M. Enhanced Dynamic Adhesion in Nematic Liquid Crystal Elastomers. *Adv. Mater.* **2019**, *31*, 1902642.
- (17) Saed, M. O.; Elmadih, W.; Terentjev, A.; Chronopoulos, D.; Williamson, D.; Terentjev, E. M. Impact Damping and Vibration Attenuation in Nematic Liquid Crystal Elastomers. *Nat. Commun.* **2021**, *12*, 6676.
- (18) Luo, C.; Chung, C.; Traugott, N. A.; Yakacki, C. M.; Long, K. N.; Yu, K. 3D Printing of Liquid Crystal Elastomer Foams for Enhanced Energy Dissipation Under Mechanical Insult. *ACS Appl. Mater. Interfaces* **2021**, *13*, 12698–12708.
- (19) Prévôt, M. E.; Ustunel, S.; Hegmann, E. Liquid Crystal Elastomers—A Path to Biocompatible and Biodegradable 3D-LCE Scaffolds for Tissue Regeneration. *Materials* **2018**, *11*, 377.
- (20) Turiv, T.; Krieger, J.; Babakhanova, G.; Yu, H.; Shiyankovskii, S. V.; Wei, Q.-H.; Kim, M.-H.; Lavrentovich, O. D. Topology Control of Human Fibroblast Cells Monolayer by Liquid Crystal Elastomer. *Sci. Adv.* **2020**, *6*, No. eaaz6485.
- (21) Agrawal, A.; Chen, H.; Kim, H.; Zhu, B.; Adetiba, O.; Miranda, A.; Cristian Chipara, A.; Ajayan, P. M.; Jacot, J. G.; Verduzco, R. Electromechanically Responsive Liquid Crystal Elastomer Nanocomposites for Active Cell Culture. *ACS Macro Lett.* **2016**, *5*, 1386–1390.
- (22) Lu, H.-F.; Wang, M.; Chen, X.-M.; Lin, B.-P.; Yang, H. Interpenetrating Liquid-Crystal Polyurethane/Polyacrylate Elastomer with Ultrastrong Mechanical Property. *J. Am. Chem. Soc.* **2019**, *141*, 14364–14369.
- (23) Lin, X.; Zou, W.; Terentjev, E. M. Double Networks of Liquid-Crystalline Elastomers with Enhanced Mechanical Strength. *Macromolecules* **2022**, *55*, 810–820.
- (24) Annapooranan, R.; Wang, Y.; Cai, S. Highly Durable and Tough Liquid Crystal Elastomers. *ACS Appl. Mater. Interfaces* **2022**, *14*, 2006–2014.
- (25) Lee, J. H.; Bae, J.; Hwang, J. H.; Choi, M. Y.; Kim, Y. S.; Park, S.; Na, J. H.; Kim, D. G.; Ahn, S. k. Robust and Reprocessable Artificial Muscles Based on Liquid Crystal Elastomers with Dynamic Thiourea Bonds. *Adv. Funct. Mater.* **2021**, *32*, 2110360.
- (26) Pei, Z.; Yang, Y.; Chen, Q.; Terentjev, E. M.; Wei, Y.; Ji, Y. Mouldable Liquid-Crystalline Elastomer Actuators with Exchangeable Covalent Bonds. *Nat. Mater.* **2014**, *13*, 36–41.
- (27) Wang, Z.; Cai, S. Recent Progress in Dynamic Covalent Chemistries for Liquid Crystal Elastomers. *J. Mater. Chem. B* **2020**, *8*, 6610–6623.
- (28) Wu, Y.; Wei, Y.; Ji, Y. Polymer Actuators Based on Covalent Adaptable Networks. *Polym. Chem.* **2020**, *11*, 5297–5320.
- (29) Saed, M. O.; Gablier, A.; Terentjev, E. M. Exchangeable Liquid Crystalline Elastomers and Their Applications. *Chem. Rev.* **2022**, *122*, 4927–4945.
- (30) Noda, Y.; Hayashi, Y.; Ito, K. From Topological Gels to Slide-Ring Materials. *J. Appl. Polym. Sci.* **2014**, *131*, 40509.
- (31) Ito, K. Slide-Ring Materials using Topological Supramolecular Architecture. *Curr. Opin. Solid State Mater. Sci.* **2010**, *14*, 28–34.
- (32) Liu, C.; Morimoto, N.; Jiang, L.; Kawahara, S.; Noritomi, T.; Yokoyama, H.; Mayumi, K.; Ito, K. Tough Hydrogels with Rapid Self-Reinforcement. *Science* **2021**, *372*, 1078–1081.
- (33) Mayumi, K.; Liu, C.; Yasuda, Y.; Ito, K. Softness, Elasticity, and Toughness of Polymer Networks with Slide-Ring Cross-Links. *Gels* **2021**, *7*, 91.
- (34) Hart, L. F.; Hertzog, J. E.; Rauscher, P. M.; Rawe, B. W.; Tranquilli, M. M.; Rowan, S. J. Material Properties and Applications of Mechanically Interlocked Polymers. *Nat. Rev. Mater.* **2021**, *6*, 508–530.
- (35) Ito, K. Novel Entropic Elasticity of Polymeric Materials: Why is Slide-Ring Gel so Soft? *Polym. J.* **2012**, *44*, 38–41.
- (36) Zheng, S. Y.; Liu, C.; Jiang, L.; Lin, J.; Qian, J.; Mayumi, K.; Wu, Z. L.; Ito, K.; Zheng, Q. Slide-Ring Cross-Links Mediated Tough Metallosupramolecular Hydrogels with Superior Self-Recoverability. *Macromolecules* **2019**, *52*, 6748–6755.
- (37) Choi, S.; Kwon, T.-w.; Coskun, A.; Choi, J. W. Highly Elastic Binders Integrating Polyrotaxanes for Silicon Microparticle Anodes in Lithium Ion Batteries. *Science* **2017**, *357*, 279–283.
- (38) Seo, J.; Lee, G. H.; Hur, J.; Sung, M. C.; Seo, J. H.; Kim, D. W. Mechanically Interlocked Polymer Electrolyte with Built-In Fast Molecular Shuttles for All-Solid-State Lithium Batteries. *Adv. Energy Mater.* **2021**, *11*, 2102583.
- (39) Minato, K.; Mayumi, K.; Maeda, R.; Kato, K.; Yokoyama, H.; Ito, K. Mechanical Properties of Supramolecular Elastomers Prepared from Polymer-Grafted Polyrotaxane. *Polymer* **2017**, *128*, 386–391.
- (40) Seo, J.; Hur, J.; Kim, M.-S.; Lee, T.-G.; Seo, S. J.; Han, S. H.; Seo, J.-H. All-Organic Piezoelectric Elastomer Formed through the Optimal Cross-Linking of Semi-Crystalline Polyrotaxanes. *Chem. Eng. J.* **2021**, *426*, 130792.
- (41) Seo, J.; Kim, B.; Kim, M.-S.; Seo, J.-H. Optimization of Anisotropic Crystalline Structure of Molecular Necklace-like Polyrotaxane for Tough Piezoelectric Elastomer. *ACS Macro Lett.* **2021**, *10*, 1371–1376.
- (42) Yoon, H.-H.; Kim, D.-Y.; Jeong, K.-U.; Ahn, S.-k. Surface Aligned Main-Chain Liquid Crystalline Elastomers: Tailored Properties by the Choice of Amine Chain Extenders. *Macromolecules* **2018**, *51*, 1141–1149.
- (43) Kim, B.; Park, T.; Oh, S. J.; Seo, J.-H. Ion-Conducting, Supramolecular Crosslinked Elastomer with a Wide Linear Range of Strain Resistances. *ACS Appl. Polym. Mater.* **2021**, *3*, 5012–5021.
- (44) Kim, K.; Guo, Y.; Bae, J.; Choi, S.; Song, H. Y.; Park, S.; Hyun, K.; Ahn, S. K. 4D Printing of Hygroscopic Liquid Crystal Elastomer Actuators. *Small* **2021**, *17*, 2100910.
- (45) Qin, H.; Mather, P. T. Combined One-Way and Two-Way Shape Memory in a Glass-Forming Nematic Network. *Macromolecules* **2009**, *42*, 273–280.
- (46) Merkel, D. R.; Shaha, R. K.; Yakacki, C. M.; Frick, C. P. Mechanical Energy Dissipation in Polydomain Nematic Liquid Crystal Elastomers in Response to Oscillating Loading. *Polymer* **2019**, *166*, 148–154.
- (47) Wang, J.; Zhao, X.; Wang, W.; Geng, X.; Zhang, L.; Guo, B.; Nishi, T.; Hu, G.-H. Significantly Improving Strength and Damping Performance of Nitrile Rubber via Incorporating Sliding Graft Copolymer. *Ind. Eng. Chem. Res.* **2018**, *57*, 16692–16700.
- (48) Saed, M. O.; Ambulo, C. P.; Kim, H.; De, R.; Raval, V.; Searles, K.; Siddiqui, D. A.; Cue, J. M. O.; Stefan, M. C.; Shankar, M. R.; Ware, T. H. Molecularly-Engineered, 4D-Printed Liquid Crystal Elastomer Actuators. *Adv. Funct. Mater.* **2019**, *29*, 1806412.
- (49) Jiang, L.; Liu, C.; Mayumi, K.; Kato, K.; Yokoyama, H.; Ito, K. Highly Stretchable and Instantly Recoverable Slide-Ring Gels Consisting of Enzymatically Synthesized Polyrotaxane with Low Host Coverage. *Chem. Mater.* **2018**, *30*, 5013–5019.
- (50) Ahn, S.-k.; Deshmukh, P.; Kasi, R. M. Shape Memory Behavior of Side-Chain Liquid Crystalline Polymer Networks Triggered by Dual Transition Temperatures. *Macromolecules* **2010**, *43*, 7330–7340.
- (51) Ahn, S.-k.; Kasi, R. M. Exploiting Microphase-Separated Morphologies of Side-Chain Liquid Crystalline Polymer Networks for Triple Shape Memory Properties. *Adv. Funct. Mater.* **2011**, *21*, 4543–4549.
- (52) Xie, T. Tunable Polymer Multi-Shape Memory Effect. *Nature* **2010**, *464*, 267–270.

(53) Zhao, Q.; Behl, M.; Lendlein, A. Shape-Memory Polymers with Multiple Transitions: Complex Actively Moving Polymers. *Soft Matter* **2013**, *9*, 1744–1755.

(54) Ahn, S.-k.; Deshmukh, P.; Gopinadhan, M.; Osuji, C. O.; Kasi, R. M. Side-Chain Liquid Crystalline Polymer Networks: Exploiting Nanoscale Smectic Polymorphism To Design Shape-Memory Polymers. *ACS Nano* **2011**, *5*, 3085–3095.

(55) Wang, Z.; He, Q.; Wang, Y.; Cai, S. Programmable Actuation of Liquid Crystal Elastomers via “Living” Exchange Reaction. *Soft Matter* **2019**, *15*, 2811–2816.

(56) Wen, Z.; Zhang, T.; Hui, Y.; Wang, W.; Yang, K.; Zhou, Q.; Wang, Y. Elaborate Fabrication of Well-Defined Side-Chain Liquid Crystalline Polyurethane Networks with Triple-Shape Memory Capacity. *J. Mater. Chem. A* **2015**, *3*, 13435–13444.

(57) Chen, Q.; Li, W.; Wei, Y.; Ji, Y. Reprogrammable 3D Liquid-Crystalline Actuators with Precisely Controllable Stepwise Actuation. *Adv. Intell. Syst.* **2021**, *3*, 2000249.

(58) Chen, Y.; Chen, C.; Rehman, H. U.; Zheng, X.; Li, H.; Liu, H.; Hedenqvist, M. S. Shape-Memory Polymeric Artificial Muscles: Mechanisms, Applications and Challenges. *Molecules* **2020**, *25*, 4246.

(59) Lee, J.; Guo, Y.; Choi, Y.-J.; Jung, S.; Seol, D.; Choi, S.; Kim, J.-H.; Kim, Y.; Jeong, K.-U.; Ahn, S.-k. Mechanically Programmed 2D and 3D Liquid Crystal Elastomers at Macro- and Microscale via Two-Step Photocrosslinking. *Soft Matter* **2020**, *16*, 2695–2705.

(60) Kobayashi, Y.; Zheng, Y.; Takashima, Y.; Yamaguchi, H.; Harada, A. Physical and Adhesion Properties of Supramolecular Hydrogels Cross-linked by Movable Cross-linking Molecule and Host-guest Interactions. *Chem. Lett.* **2018**, *47*, 1387–1390.

(61) Nakahata, M.; Mori, S.; Takashima, Y.; Yamaguchi, H.; Harada, A. Self-Healing Materials Formed by Cross-Linked Polyrotaxanes with Reversible Bonds. *Chem* **2016**, *1*, 766–775.

(62) Luo, X.; Mather, P. T. Shape Memory Assisted Self-Healing Coating. *ACS Macro Lett.* **2013**, *2*, 152–156.



CAS BIOFINDER DISCOVERY PLATFORM™

ELIMINATE DATA SILOS. FIND WHAT YOU NEED, WHEN YOU NEED IT.

A single platform for relevant, high-quality biological and toxicology research

Streamline your R&D

CAS
A division of the American Chemical Society

The advertisement features a vertical strip on the left showing a 3D molecular model with various colored spheres (grey, orange, blue, green) connected by lines, set against a background of green and orange gradients. The main text is on a dark blue background.